Understanding electron transport mechanisms in monolayer MoS_2 transistors: Impact of lattice phonon scattering and localized charge traps

Yakui Mu [1], Siyu Liu [1], Yanming Wang [2], Zhikun Liu,[1,*] and Mingzhen Zhao [1,†]

[1] *School of Mechanical Engineering, Shanghai Jiao Tong University, Shanghai 200240, China*

[2] *University of Michigan–Shanghai Jiao Tong University Joint Institute, Shanghai Jiao Tong University, Shanghai 200240, China*

(Received 13 June 2024; revised 25 July 2024; accepted 20 August 2024; published 9 September 2024)

Monolayer molybdenum disulfide (MoS_2) is a prominent two-dimensional semiconductor material known for its high theoretical intrinsic mobility. However, when implemented in transistors, the mobility significantly decreases. To investigate the mechanisms behind this reduction, several theoretical models have been developed to correlate device mobility with temperature. Despite these efforts, the accuracy of existing models remains limited due to the simplified calculation for lattice phonon scattering limited mobility (μ_{ph}) and lack of appropriate temperature consideration for the localized charge trap (LCT) effect. In this paper, we present a theoretical model to address the mobility degradation in monolayer MoS_2 transistors by thoroughly reevaluating μ_{ph} and the LCT effect. The temperature and electron concentration dependence of μ_{ph} was calculated with full *ab initio* scattering rates in the Boltzmann transport equation framework. Additionally, the temperature-dependent parameters (energy range and density of LCT) were proposed to evaluate the LCT effect rationally. Our model accurately fits various electron transport mechanisms for monolayer MoS_2 transistors, particularly those dominated by lattice phonon scattering or dominated by LCT effects. The validation and broad applicability of the model offer a robust approach for quantitatively analyzing the electron transport mechanisms of monolayer MoS_2 transistors.

DOI: 10.1103/PhysRevB.110.115414

I. INTRODUCTION

In the postsilicon era, mobility degradation is a major challenge in bulk semiconductors, due to limited channel thickness [1]. Monolayer transition metal dichalcogenides (TMDs) comprise a category of two-dimensional (2D) semiconductor materials, which is one of the promising candidates to address the issue [2–5]. Monolayer molybdenum disulfide (MoS_2), as a representative of TMDs, exhibits dangling-bond-free surfaces, alternative band gaps, and robust designability [6–8], which could be applied in transistors [4,9,10], optical devices [11,12], memristive devices [13–15], and sensors [16,17], etc. In an early study, it was shown that monolayer MoS_2 has a high theoretical intrinsic mobility of 410 $cm^2\,V^{-1}\,s^{-1}$ at room temperature [18]. However, when implemented in semiconductor transistors, the typical mobilities of monolayer MoS_2 transistors are only 5−30 $cm^2\,V^{-1}\,s^{-1}$ [19–22]. Strategies that involve improving material quality and/or interfacial environment could raise the mobility to 60−148 $cm^2\,V^{-1}\,s^{-1}$ [23–26]. To resolve the mobility discrepancy, theoretically understanding the electron transport mechanisms of monolayer MoS_2 transistors is essential.

In recent years, researchers have conducted several studies, attributing the mobility degradation of monolayer MoS_2 primarily to lattice defects, interfacial Coulomb impurities (CIs), surface optical (SO) phonons, and physical or chemical adsorbates, etc. [20,22,24,27,28]. Theoretical models have also been developed based on Matthiessen's rule to bridge device mobility-temperature relationships with these obstacles [23,29]. Ma *et al.* [30] studied individual scattering mechanisms and concluded that the most important external limitation is CI scattering. Yu *et al.* [23,24] comprehensively analyzed the effect of the improved quality of monolayer MoS_2 and increased dielectric constant on electron transport mechanisms. While the reported models are operational in the majority of cases, there are still some situations that need to be addressed. For instance, the hexagonal BN (h-BN) encapsulated monolayer MoS_2 transistor exhibits high temperature-dependent mobility, but there are some deviations in the fitting results [20,27]. The mobility of some exfoliated and CVD-grown MoS_2 monolayers showed an increasing and subsequently decreasing trend with increasing temperature, which needs to be explained by better fitting results [23,31,32]. We then conducted some surveys of existing models.

The lattice phonon scattering limited mobility (μ_{ph}) is calculated as a part of the total device mobility in the model. The reported models estimated μ_{ph} of monolayer MoS_2 to be ∼410 $cm^2\,V^{-1}\,s^{-1}$ at room temperature [20,23,24,33–35]. However, the calculation method is limited and simplified, primarily in three aspects: (1) A simple basis set was applied [linear combination of atomic orbitals (LCAO)], which is commonly used to describe nonperiodic systems [35,36]. (2) The frozen-phonon (FP) method (also called constant deformation potential) was utilized to ignore the anisotropy of electron-phonon (e-ph) matrix elements in monolayer MoS_2 crystal [35–37]. (3) The scattering processes and e-ph matrix elements involve only a few states. This approach can lead to

*Contact author: liuzhikun@sjtu.edu.cn

†Contact author: zhaomz@sjtu.edu.cn

deviated results or even failure to converge [35–39]. In recent years, these issues have been recognized and progressively addressed [40–46]. For instance, Zhou *et al.* [45] developed a postprocessing program (PERTURBO code), in conjunction with QUANTUM ESPRESSO (QE) codes, to consider the above issues and calculated the mobility of monolayer MoS_2 as 168 $cm^2\ V^{-1}\ s^{-1}$ at room temperature. The initial calculation results for μ_{ph} reported by Kaasbjerg *et al.* [35] were >2 times the values reported by Zhou *et al.* [45]. According to Matthiessen's rule, the overestimation of μ_{ph} directly results in the underestimation of the other components. The overestimation of μ_{ph} may be one reason the theoretical values do not align well with the experimental results. However, the improved calculation method for μ_{ph} has not yet been integrated into the model to analyze the experimental mobility of monolayer MoS_2 transistors.

Another important aspect is to rationally evaluate the localized charge trap (LCT) effect. In practice, both structural defects in materials and physical or chemical adsorption during the fabrication process introduce LCT states in the band gap of monolayer MoS_2 [23,31,47,48]. In general, the concept of mobility edge in the conduction band tail was proposed in previous studies to introduce the LCT effect [23,31]. The states above the mobility edge are called extended states with band transport. The remaining localized states transport through the thermally assisted mode. If the LCT effect is not considered in the theoretical model, it would lead to an underestimation of scattering limited mobilities. Additionally, the LCT density varies with temperature, which is needed to be reflected in the modeling. Recently, Joo *et al.* [32,49] revealed that the interfacial trap density of monolayer MoS_2 transistors decreases noticeably with temperature. Park *et al.* [50] experimentally observed a thermally activated trap density with temperature increasing from 10 to 300 K in a multilayer MoS_2 field-effect transistor. This experimental evidence implies that the variation of LCT-related parameters with temperature should be considered in the theoretical model.

In this paper, we developed a theoretical model to decouple experimental mobilities of monolayer MoS_2 transistors, which in turn provides insights into the electron transport mechanisms in different systems. We adopt the PERTURBO calculation method for reevaluating μ_{ph} and further integrate the term into our model. The LCT effect was considered during the all-fitting process. Moreover, temperature-dependent parameters (energy range and density of LCT) were proposed and implemented in our case studies. The reevaluation of lattice phonon scattering and the LCT effect is expected to provide more accurate fitting results and enhace our understanding of the mobility discrepancy between monolayer MoS_2 and corresponding transistors.

II. METHODS

Electron transport of monolayer MoS_2 transistors can be theoretically decoupled on the basis of Matthiessen's rule and the LCT effect [27,29,30]. The effective mobility (μ_{eff}) is given as

$$\mu_{\text{eff}} = \mu_0 \frac{\partial n_{\text{band}}}{\partial n} = \left(\mu_{\text{ph}}^{-1} + \mu_{\text{CI}}^{-1} + \mu_{\text{SO}}^{-1}\right)^{-1} \frac{\partial n_{\text{band}}}{\partial n}, \quad (1)$$

where μ_0 is the mobility of free electrons; $\frac{\partial n_{\text{band}}}{\partial n}$ is defined to quantify the magnitude of the LCT effect that is caused by structural defects, physical or chemical adsorbates, etc.; n is the total electron concentration; n_{band} is the electron concentration of extended states; and μ_{ph}, μ_{CI}, and μ_{SO} are the mobilities limited by lattice phonon scattering, CI scattering, and SO phonon scattering, respectively.

Next, we briefly introduce the main features of each part. The calculation details can be found in the Supplemental Material [51] (including Refs. [3,8,22–25,30,31,35,45,47,48,52–67]).

A. Calculation of lattice phonon scattering limited mobility (μ_{ph})

QE codes were utilized to compute the electronic and phononic structure as well as electron-phonon interactions of monolayer MoS_2 [54–56]. The generalized gradient approximation (GGA) [61] was used for the exchange-correlation potential. The kinetic energy cutoff was 80 Ry, and the convergence threshold on total energy and forces were 10^{-4} and 10^{-8} a.u., respectively. The spin-orbit coupling (SOC) effects [8] and the truncation of the Coulomb interaction in the z direction [63,64] were also considered in all calculations. The WANNIER90 (W90) code [57,58,62,65] was employed to obtain localized Wannier functions. Subsequently, the electronic structure and phonon dispersion were interpolated by the PERTURBO code [45]. Here, μ_{ph}-T relationships at different carrier concentrations of monolayer MoS_2 were then derived by solving the Boltzmann transport equation with the relaxation time approximation in the PERTURBO code.

B. Calculation of CI and SO scattering limited mobilities (μ_{CI} and μ_{SO})

Regarding μ_{CI} and μ_{SO}, the calculation process is similar. First, the scattering rate was calculated based on Fermi's golden rule, and then the mobility was solved using the Boltzmann transport equation within the relaxation-time approximation [60].

The scattering rate of CI scattering can be written as follows [30,53]:

$$\Gamma_{\text{imp}}(E_k) = \frac{n_{\text{imp}}}{2\pi\hbar} \int dk' \left|\phi^{\text{scr}}_{|k-k'|}\right|^2 (1 - \cos\theta_{kk'}) \delta(E_k - E_{k'}), \quad (2)$$

where n_{imp} is the concentration of CI, Φ_q^{scr} is the screened CI potential, E_k and $E_{k'}$ are the energies corresponding to the momentum wave vectors before and after CI scattering, and $\theta_{kk'}$ is the scattering angle.

As for the scattering rate of SO phonons, The expression can be shown as follows [24]:

$$\Gamma^{\pm}_{\text{so}}(E) = \frac{e^2 \omega_{\text{so}} m_{\text{eff}}}{8\pi\hbar^2} \left(\frac{1}{2} \pm \frac{1}{2} + N_{\text{so}}\right) \int_{-\pi}^{\pi} d\theta \frac{1 - \frac{k'}{k}\cos\theta}{q} \times \left[\frac{1}{\varepsilon^{\infty}_{\text{tot,SO}} + \varepsilon_{\text{el}}(q)} - \frac{1}{\varepsilon^{0}_{\text{tot,SO}} + \varepsilon_{\text{el}}(q)}\right], \quad (3)$$

where + and − represent SO phonon emission and adsorption, ω_{SO} is the frequency of SO phonons, m_{eff} is the effective electron mass, N_{so} is Bose-Einstein distribution of SO phonons,

TABLE I. Summarized mobility values of monolayer MoS_2 devices from previous studies and this paper. The calculation methods for electronic structure and e-ph matrix elements are also shown in this table. Abbreviations not already defined in text: Perdew-Burke-Ernzerhof (PBE), optimized norm-conserving Vanderbilt (ONCV), linear interpolation (LI), Wannier interpolation (WI).

Year published	Mobility ($cm^2\ V^{-1}\ s^{-1}$)		Electronic structure	e-ph matrix elements	Vacuum spacing (Å)	Ref.
	Intrinsic	$n = 2 \times 10^{12}\ cm^{-2}$				
2012	410	387[a]	LCAO, LDA	FP	10	[35]
2016	380	368[a]	LCAO, PBE	FP (9×9)	30	[36]
2022	274	264[a]	PW, PBE	FP (9×9)	20	[37]
2013	320	–	PW, LDA	DFPT	–	[38]
2014	225	–	PW, PBE	DFPT	–	[39]
2015	150	–	PW, PBE	DFPT+LI	–	[40]
2018	47	45[a]	PW, ONCV-LDA	DFPT+WI	15	[41]
2019	97	–	ONCV-PBE	DFPT+WI	14	[42]
2019	101	–	ONCV-PBE	DFPT+WI	14	[43]
2021	145	–	PW, ONCV-PBE+SOC	DFPT+WI	–	[44]
2021	–	168	PW, ONCV-PBE+SOC+ 2D polar corrections	DFPT+WI	17+ Coulomb truncation	[45]
2022	158	–	ONCV-PBE	DFPT+WI	20	[46]
–	182	175	PW, ONCV-PBE+SOC+2D polar corrections	DFPT+WI	16+ Coulomb truncation	This paper

[a]Extracted values from papers.

$\varepsilon^{\infty}_{tot,SO}$ and $\varepsilon^{0}_{tot,SO}$ are the optical and static dielectric response of the interface, and $\varepsilon_{el}(q)$ is the electronic part of the generalized static dielectric function.

C. Calculation of LCT effect

Due to the presence of LCTs, the electron concentration (n) is divided into two parts [23,67]:

$$n = n_{band} + n_{loc} = \int_0^{+\infty} D_0 f(E) dE + \int_{-\Delta E_{tr}}^{0} \frac{N_{tr}}{\Delta E_{tr}} f(E) dE, \tag{4}$$

where n_{band} and n_{loc} are the concentrations of the extended states and the localized states, D_0 is the density of states in the conduction band, $f(E)$ is equilibrium Fermi-Dirac distribution function, and ΔE_{tr} and N_{tr} are the energy range and density of the LCT effect.

III. RESULTS AND DISCUSSION

Here, μ_{ph} reflects the intrinsic transport behavior of monolayer MoS_2 crystal. As described in the Introduction section, the initial calculations overestimated μ_{ph} due to the method limitations. With the improved calculation methods, the calculated μ_{ph} is close to the experimental results ($148\ cm^2\ V^{-1}\ s^{-1}$) for structural and interfacial optimization [24]. As shown in Table I, the development of μ_{ph} at room temperature involves three main stages: (1) Gaddemane *et al.* [44] employed a plane-wave (PW) basis set instead of the originally applied LCAO basis set ($380\ cm^2\ V^{-1}\ s^{-1}$ [36]), and calculated the mobility of $274\ cm^2\ V^{-1}\ s^{-1}$ [37]. The improvement of the stage is to enable the basis set more compatible with the periodic system. (2) Li *et al.* [38] and Restrepo *et al.* [39] utilized density functional perturbation theory (DFPT) to calculate full e-ph matrix elements instead of the FP method, which provides a more realistic consideration of the anisotropy of e-ph matrix elements in monolayer MoS_2 crystal. The calculated mobilities were $320\ cm^2\ V^{-1}\ s^{-1}$ with local density approximation (LDA) and $225\ cm^2\ V^{-1}\ s^{-1}$ with GGA. (3) In recent years, the QE code combined with the postprocessor method has been developed to achieve interpolation of the Wannier function on fine grids instead of a coarse grid, which effectively avoids the situations of deviated results or even failure to converge. Li *et al.* [40] and Gaddemane *et al.* [44] calculated the mobility using the Monte Carlo program method to be 150 and $147\ cm^2\ V^{-1}\ s^{-1}$, respectively. Song *et al.* [46] calculated a comparable mobility value ($158\ cm^2\ V^{-1}\ s^{-1}$) using the Electron-phonon Wannier (EPW) method, which is comparable with experimental results. In addition, we note some significantly lower values calculated by the QE+EPW method. For example, the mobility calculated by Zhao *et al.* [41] is only $47\ cm^2\ V^{-1}\ s^{-1}$. We assume that this may be related to the adopted LDA exchange-correlation function [44]. The mobilities calculated by Guo *et al.* [42,43] (97 and $101\ cm^2\ V^{-1}\ s^{-1}$, respectively) were also inappropriate and obviously lower than those of Song *et al.* [46], where a similar method was utilized. This result is close to the mobility of bulk MoS_2 ($97.1\ cm^2\ V^{-1}\ s^{-1}$ [46]). One possible reason is that a smaller vacuum distance in the z-axis direction has been adopted, which affects charge transport via Coulombic interactions [63]. Recently, Zhou *et al.* [45] developed the PERTURBO code that supports SOC, polar corrections, and Coulombic truncation for 2D materials, which allows monolayer MoS_2 to obtain a mobility value of $168\ cm^2\ V^{-1}\ s^{-1}$ at $n = 2 \times 10^{12}\ cm^{-2}$. In comparison with the references utilizing the EPW method, the authors utilizing the PERTURBO

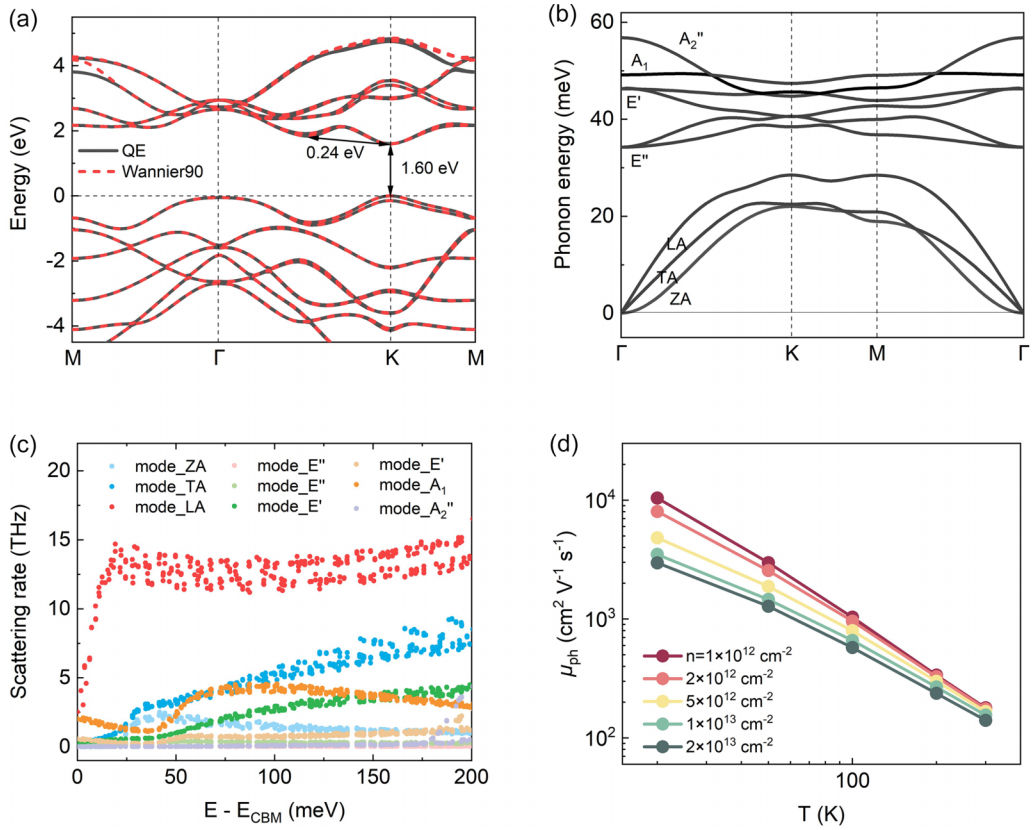

FIG. 1. Calculated (a) electronic and (b) phononic structures of monolayer MoS_2. (c) Mode-resolved e-ph scattering rates at room temperature. The energy zero represents the energy corresponding to the conduction band minimum of monolayer MoS_2. (d) Temperature dependence of μ_{ph} with n ranging from 1×10^{12} to 2×10^{13} cm^{-2} at temperatures of 20, 50, 100, 200, and 300 K.

method simultaneously considered the SOC effects, the e-ph polar corrections for 2D materials, and the Coulomb interaction truncation in the z direction, which made the calculated mobilities of monolayer MoS_2 more reasonable.

Figures 1(a) and 1(b) show the calculated electronic and phononic structure of monolayer MoS_2. To compute the electron energy and band velocity more efficiently, we used the W90 code [57,58,62,65] to obtain localized Wannier functions of monolayer MoS_2 on the same k-point grid [red dotted lines in Fig. 1(a)]. In addition, we resolved the scattering rates of different phonon modes by utilizing the PERTURBO code. As shown in Fig. 1(c), the longitudinal acoustic (LA) phonon mode dominates the lattice phonon scattering of monolayer MoS_2 at room temperature. Figure 1(d) illustrates the μ_{ph}-T relationships ($T = 20$, 50, 100, 200, and 300 K) with n varing from 1×10^{12} to 2×10^{13} cm^{-2}. Generally, μ_{ph} decreases with increasing T due to the more intense phonon number in MoS_2 at elevated T [22]. At a given temperature, μ_{ph} decreases with increasing n due to the higher probability of collision, which hinders electron transport. In addition, the value of μ_{ph} exhibits a weaker n dependence as T increases. For instance, at $T = 20$ K, μ_{ph} ranges from 10 411 to 2963 $cm^2\,V^{-1}\,s^{-1}$ as n increases from 1×10^{12} to 2×10^{13} cm^{-2}, which is a notably larger range than that of 300 K, where it varies from 179 to 141 $cm^2\,V^{-1}\,s^{-1}$.

As μ_{CI} is calculated based on a predefined device structure and parameters, for the sake of discussion, we designate the monolayer MoS_2 transistors as a top-gate structure. The substrate is silicon oxide with infinite thickness. A dielectric layer is aluminum oxide (Al_2O_3) with a thickness of 30 nm. Here, n_{CI} is assumed to be 1×10^{12} cm^{-2}. CI centers have Coulomb interactions with electrons, consequently impeding the transport process. In the meantime, dielectric materials and free electrons screen the CI centers, facilitating the electron transport process. The interaction potential can be described as $\Phi_q^{scr}(z=0) = \frac{\Phi_q(0)}{\varepsilon_{2D}(q,T)} = \frac{e^2 G_q(0,0)}{1-e^2 G_q(0,0)\prod(q,T,E_F)}$, where Φ_q^{scr} is the screened CI potential; $\Phi_q(0)$ and $\varepsilon_{2D}(q,T)$ are CI scattering potential and generalized static dielectric function; $G_q(0,0) = \frac{1}{q[\varepsilon_t^0 \coth(qd)+\varepsilon_b^0]}$ is the Fourier transform of the Green's function solution of the Poisson equation; ε_t^0 and ε_b^0 are the static permittivity of the top and bottom dielectric layers; d is the thickness of the top dielectric layer; and e, q, T, and E_F are the electric charge, wave vector, temperature, and chemical potential, respectively [53,59,60]. For a device with a specified n_{CI}, the magnitude of Φ_q^{scr} is closely related to the dielectric materials and electron concentration. When dielectric constant (ε) and n increase, the screening of the CI potential becomes more effective, resulting in an increased μ_{CI}. In Fig. 2(a), μ_{CI}-T relationships with different n are depicted. At a specified n, μ_{CI} decreases with increasing T due to the weakening of charge polarity at higher T, leading to reduced screening. The decrease in μ_{CI} is more pronounced at higher temperatures [24,30]. In addition, μ_{CI} shows a decreasing trend as n decreases due to weakened screening. Figure 2(b) reveals μ_{CI} as a function of the top dielectric

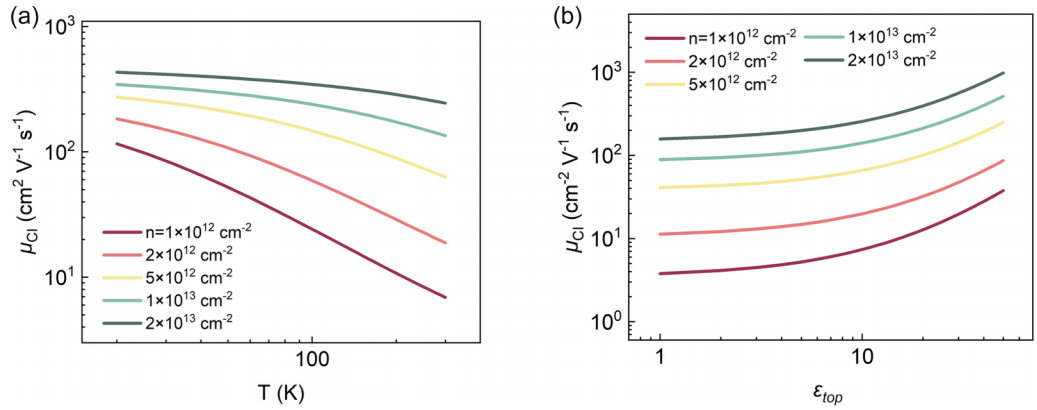

FIG. 2. (a) μ_{CI}-T relationships at $n_{CI} = 1 \times 10^{12}$ cm^{-2}. (b) μ_{CI}-ε_{top} relationships at T= 300 K. n ranges from 1×10^{12} to 2×10^{13} cm^{-2}.

constant (ε_{top}), similarly demonstrating stronger CI screening with increased ε_{top} and n.

The excited SO phonons at the interface similarly impede electron transport in the monolayer MoS_2 transistors. To investigate the impact of SO phonon scattering, we applied Al_2O_3 dielectric layer as an example. Figure 3 exhibits μ_{SO}-T relationships with different n. At low temperatures, μ_{SO} possesses a very high value, which has negligible impact on μ_{eff} according to Matthiessen's rule. For instance, at $n = 1 \times 10^{12}$ cm^{-2} and $T = 100$ K, μ_{SO} reaches 47 605 cm^2 V^{-1} s^{-1}, which is 46 times higher than μ_{ph} (1034.255 cm^2 V^{-1} s^{-1}). However, at room temperatures, SO phonon scattering becomes comparable with lattice phonon scattering (with $\mu_{SO} =$ 168 cm^2 V^{-1} s^{-1} and $\mu_{ph} = 179$ cm^2 V^{-1} s^{-1}) due to the increased coupling between SO phonons and electrons (refer to Eqs. (S8)–(S11) in the Supplemental Material [51]). In addition, μ_{SO} increases with increasing n at a given temperature, suggesting a similar electron screening effect as observed in μ_{CI}.

To analyze the LCT effect on electron transport, we assume that electrons in monolayer MoS_2 are solely influenced by lattice phonon scattering, excluding CI scattering and SO phonon scattering ($\mu'_{eff} = \mu_{ph}\frac{\partial n_{band}}{\partial n}$). Figure 4(a) demonstrates μ'_{eff} as a function of N_{tr} with various n values at room temperature. It is observed that, when $N_{tr} > n$, μ'_{eff} decreases rapidly, indicating that electron transport is increasingly dominated by the LCT effect. Moreover, $\frac{\partial n_{band}}{\partial n}$ can be used to define to quantify the magnitude of the LCT effect. Also, $\frac{\partial n_{band}}{\partial n} = 1$ indicates that electron transport is not influenced by the LCT effect, while $\frac{\partial n_{band}}{\partial n} \sim 0$ suggests that electrons are predominately confined by the significant hopping barriers. To examine the relationships between $\frac{\partial n_{band}}{\partial n}$, T, and n, we utilized mean values of N_{tr} and ΔE_{tr} ($N_{tr} = 5 \times 10^{12}$ cm^{-2} and $\Delta E_{tr} = 50$ meV) derived from the fitted parameters summarized in previous studies [27]. As shown in Fig. 4(b), $\frac{\partial n_{band}}{\partial n}$ as a function of T exhibits two distinct trends. When N_{tr} is greater than n, $\frac{\partial n_{band}}{\partial n}$ increases with T. For $T < 100$ K, the value of $\frac{\partial n_{band}}{\partial n} < 0.1$. For $T > 100$ K, the growth rate accelerates. The result indicates that the electron transport in this situation occurs mainly in a hopping manner [23,31]. When $N_{tr} < n$, $\frac{\partial n_{band}}{\partial n}$ decreases with increasing T, indicating that electron transport mainly proceeds in a band manner. It is noteworthy that the transition occurs approximately at $n = N_{tr}$.

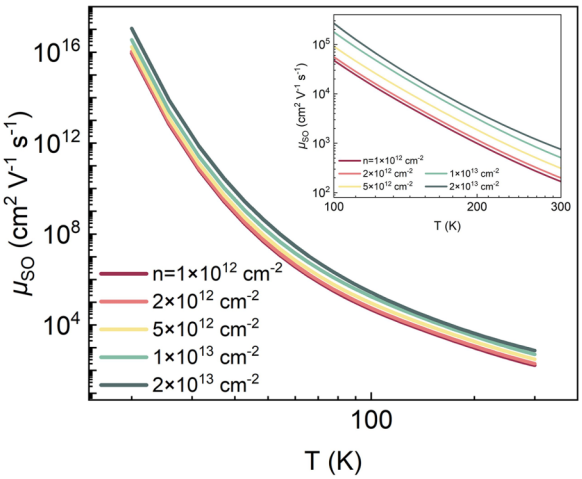

FIG. 3. μ_{SO}-T relationships with Al_2O_3 as the dielectric layer with n ranging from 1×10^{12} to 2×10^{13} cm^{-2}. The inset shows the change of μ_{SO} with T range from 100 to 300 K.

Having elucidated temperature- and electron concentration-dependent phenomena of μ_{ph}, μ_{CI}, μ_{SO}, and $\frac{\partial n_{band}}{\partial n}$ individually, Matthiessen's rule and the LCT effect were considered to integrate them and obtain μ_{eff}. Herein, the same MoS_2 device structure that introduced μ_{CI} was utilized. Also, μ_{eff}-T relationships for different n values are depicted in Fig. 5(a). For $n < N_{tr}$, μ_{eff}-T presents an insulating behavior dominated by the LCT effect [23,31,68]. However, for $n > N_{tr}$, the LCT effect diminishes, which results in a scattering-limited band behavior. CI scattering is the dominant limited mechanism for μ_{eff} at low T. The relationships between μ_{eff} and n_{CI} are presented in Fig. 5(b). Meanwhile, the lower the n, the more pronounced the decrease in μ_{eff}. Figure 5(c) illustrates μ_{eff}-ε_{top} relationships at $T = 300$ K with different n values. Here, μ_{eff} shows an increasing trend with increasing ε_{top} and n. This is mainly because increasing ε_{top} and n can improve μ_{CI} due to the enhanced screening of the CI potential, which in turn improves μ_{eff} according to Matthiessen's rule. Figure 5(d) represents μ_{eff}-N_{tr} relationships at $T = 300$ K with different n values. Differently introduced in Fig. 5, both CI and SO scattering were considered. Here, μ_{eff} decreases

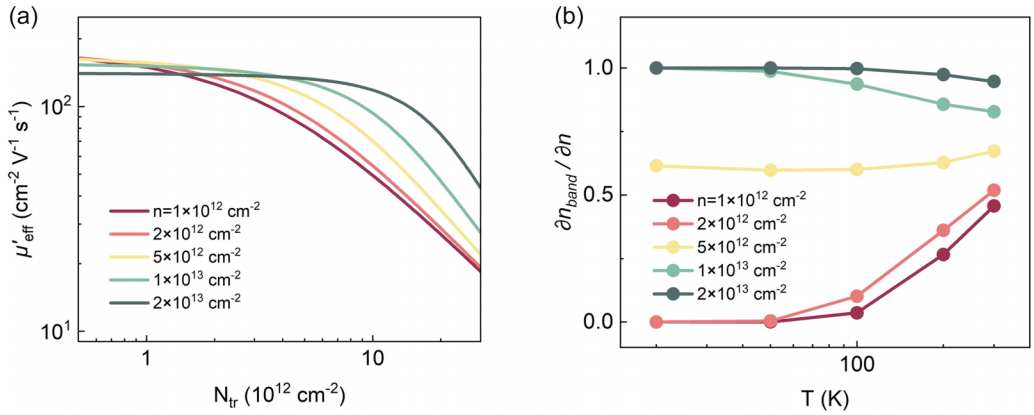

FIG. 4. μ'_{eff}-N_{tr} relationships at $n_{\text{CI}} = 1 \times 10^{12}\,\text{cm}^{-2}$ and $T = 300$ K when only ph scattering is considered. $\frac{\partial n_{\text{band}}}{\partial n}$-$T$ relationships at $N_{\text{tr}} = 5 \times 10^{12}\,\text{cm}^{-2}$ and $\Delta E_{\text{tr}} = 50$ meV at temperatures of 20, 50, 100, 200, and 300 K.

monotonically as N_{tr} increases. Specifically, when $N_{\text{tr}} > n$, the LCT effect becomes the major constraint, with μ_{eff} decreasing rapidly as N_{tr} increases.

To verify the applicability of our developed model, several published experimental data were referred, and their difference in electron transport mechanisms was analyzed. The fitted monolayer MoS_2 transistors include (1) mobility variation with both T and n, (2) improvement of material quality, and (3) modulation of interfacial environment. It is noted that the mobilities of selected cases were extracted from four-probe measurements, which is expected to avoid contact resistance as much as possible. The monolayer MoS_2 in the experimental cases originated from mechanical exfoliation.

The first experimental case involves mobility variation with both T and n reported by Radisavljevic *et al.* [3]. As shown in Fig. 6(a), the experimental data were plotted and fitted with our model, showing great consistency. The microscopic parameters (N_{tr} and n_{CI}) were extracted and shown

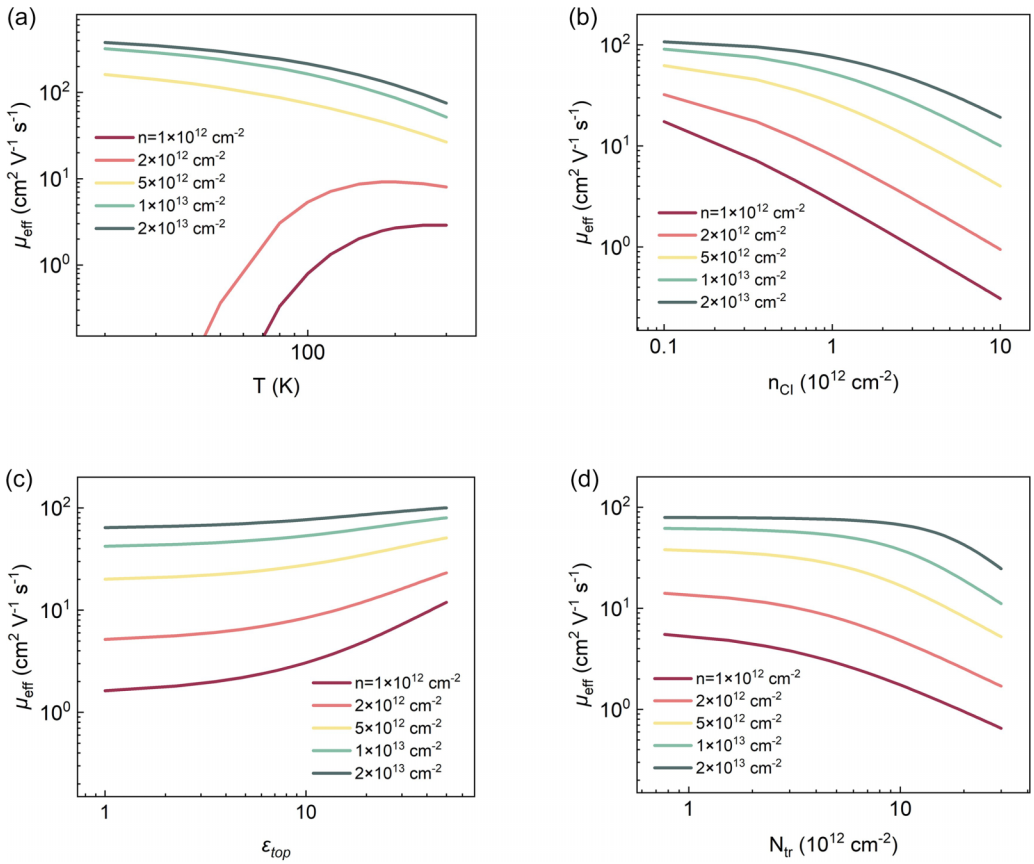

FIG. 5. Device parameters dependence of μ_{eff} with n ranging from 1×10^{12} to $2 \times 10^{13}\,\text{cm}^{-2}$. (a) μ_{eff}-T relationships at $n_{\text{CI}} = 1 \times 10^{12}\,\text{cm}^{-2}$ and $N_{\text{tr}} = 5 \times 10^{12}\,\text{cm}^{-2}$. (b) μ_{eff}-n_{CI} relationships and (c) μ_{eff}-ε_{top} relationships at $n_{\text{CI}} = 1 \times 10^{12}\,\text{cm}^{-2}$ with T= 300 K, $N_{\text{tr}} = 5 \times 10^{12}\,\text{cm}^{-2}$ and $\Delta E_{\text{tr}} = 50$ meV. (d) μ_{eff}-N_{tr} relationships at $n_{\text{CI}} = 1 \times 10^{12}\,\text{cm}^{-2}$, $T = 300$ K, and $\Delta E_{\text{tr}} = 50$ meV.

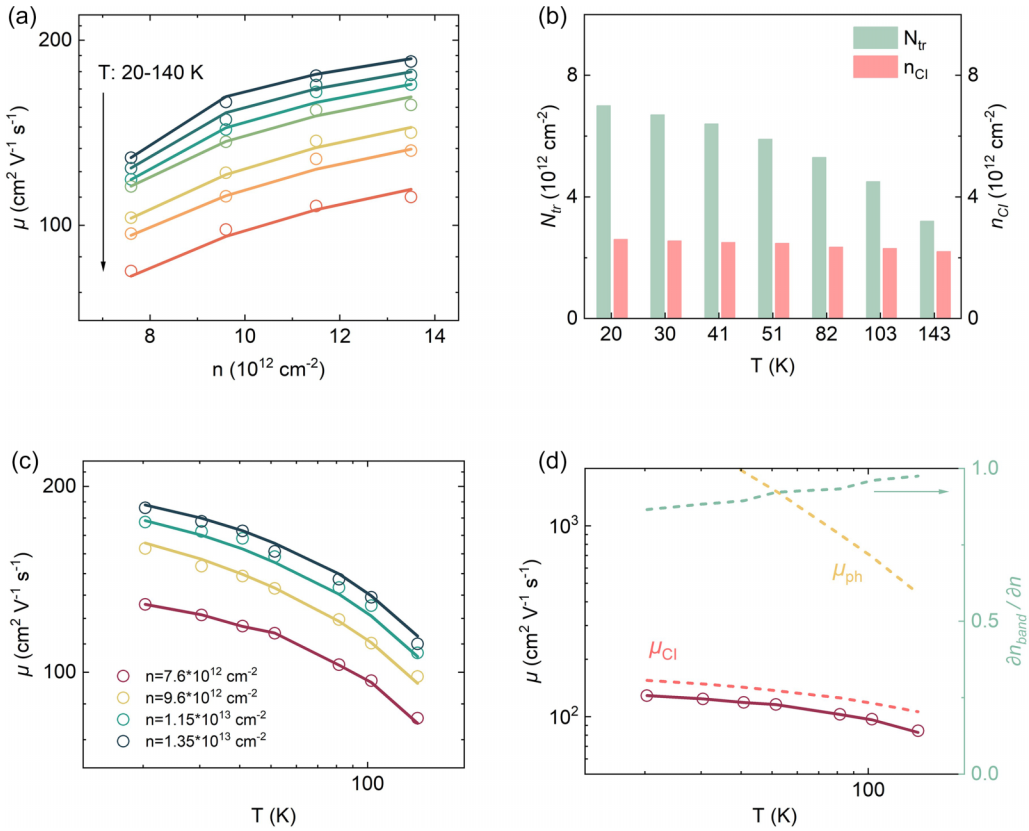

FIG. 6. (a) The μ_{ex}-n relationships (symbols) and the fitted results (solid lines) with different T varying from 20 to 143 K [3]. (b) The temperature dependence of microscope parameters of N_{tr} (light green column) and n_{CI} (pink column). (c) The μ_{ex}-T relationships (symbols) and the fitting results (solid lines) with different n (7.6×10^{12}, 9.6×10^{12}, 1.15×10^{12}, and 1.35×10^{12} cm^{-2}). (d) The μ_{ex}-T relationships (red symbols) and the fitted results (red solid lines) at $n = 7.6 \times 10^{12}$ cm^{-2}. μ_{CI}, μ_{ph}, and the localized charge trap (LCT) effect are also shown (pink, yellow, and light green dotted lines).

in Fig. 6(b). We found that n_{CI} varies little regardless of T, whereas the other two parameters (N_{tr} and ΔE_{tr}) exhibit strong temperature dependency. For instance, when T changes from 20 to 143 K, n_{CI} varies in the range of 2.6×10^{12} to 2.2×10^{12} cm^{-2}. However, N_{tr} (ΔE_{tr}) changes from 7.0×10^{12} cm^{-2} (65 meV) to 3.2×10^{12} cm^{-2} (200 meV). Since CI centers mainly originate from sulfur vacancies and charge centers at interfaces, it is reasonable that the fitted n_{CI} exhibits a small temperature dependence. The variation of N_{tr} and ΔE_{tr} (for details, refer to Table II) with temperature is mainly due to the situation that more electrons are thermally excited to the extended state as the temperature increases, which in turn shows a decrease of the trap density of states. Recently, Joo *et al.* [32,49] revealed that the interfacial trap density of a monolayer MoS_2 transistor changes with temperature, which provides experimental evidence for the variations of the microscopic parameters. Figure 6(c) presents the μ_{ex}-T relationships (symbols) and the fitting results (solid lines) with different n's derived from Fig. 6(a). Figure 6(d) shows the experimental μ_{ex}-T relationship (red symbols) and fitted curves (red solid line) at $n = 7.6 \times 10^{12}$ cm^{-2}. Scattering-limited mobilities and the LCT effect with T (pink dotted line: μ_{CI}-T, yellow dotted line: μ_{ph}-T, light green dotted line: $\frac{\partial n_{band}}{\partial n}$-$T$) are also documented. The μ_{SO}-T curve is located out of the presented μ scope (Fig. S2 in the Supplemental Material [51]), and it is not shown here for clarity. It can be seen that μ_{CI} is closest to the experimental data. According to Matthiessen's rule, the result suggests that CI scattering is the dominant limited mechanism in the entire temperature range. Lattice phonon scattering acts as a secondary limited mechanism. Additionally, $\frac{\partial n_{band}}{\partial n} \sim 1$ along with raising T, which indicates the diminishing trap confinement for electrons at higher T. The study of this case has allowed the recognition that the microscope parameters in the LCT effect are temperature dependent, which is essential for analyzing the LCT-dominated limited mechanism.

It is essential to note that the synergistic effect of temperature and electron concentration on mobility was not usually considered in prior studies. As a result, we are unable to extract the temperature-dependent parameters of the LCT effect. Therefore, we proposed a simplified modeling strategy for different temperature regions by changing only the fitted N_{tr} and ΔE_{tr} (without varying n_{CI}). In addition, 100 K was chosen as the empirical boundary between the high-temperature (HT) and low-temperature (LT) regions. It follows the facts that the conventional μ_{ex}-T relationship shows two-stage phenomena [22,23,27]. In the LT region, μ_{ex} gradually saturates with decreasing T due to the CI scattering limitation. In the HT region, μ_{ex} decreases almost linearly with increasing T due to lattice phonon scattering limitation. It needs to be pointed out that there is no clear physical meaning of this boundary. Table II details the device parameters and extracted

TABLE II. Device parameters [electron concentration (n), temperature (T), dielectric constant (ε)] and fitted parameters [CI concentration (n_{CI}), energy range and density of trap states (ΔE_{tr} and N_{tr})] of the experimental cases referenced in this paper. LT and HT represent low temperature and high temperature in which $T = 100$ K was chosen as the empirical boundary.

Sample description	n (10^{12} cm^{-2})	T (K)	Top dielectric (ε_{top})	Bottom dielectric (ε_{bottom})	n_{CI} (10^{12} cm^{-2})	N_{tr} (10^{12} cm^{-2})	ΔE_{tr} (meV)	Ref.
Top gate, exfoliated	7.6	20	19	3.9	2.6	7.0	65	[3]
		30			2.6	6.7	75	
		41			2.5	6.4	84	
		51			2.5	5.9	95	
		82			2.4	5.3	129	
		103			2.3	4.5	180	
		143			2.2	3.2	200	
Back gate, exfoliated	7.1	LT region	–	3.9	0.90	10.5	13	[23]
		HT region			0.90	10.2	45	
Back gate, exfoliated, TS treated		LT region			0.88	7.4	30	
		HT region			0.88	6.2	50	
Back gate, exfoliated, DS treated		LT region			0.23	7.4	40	
		HT region			0.23	6.6	50	
Al_2O_3-encapsulated double gate, exfoliated	10	LT region	12	12	1.9	10.2	85	[34]
		HT region			1.9	9.8	100	
HfO_2-encapsulated double gate, exfoliated	7.0	LT region	22	22	7.6	5.6	110	[20]
		HT region			7.6	6.8	110	
BN-encapsulated double gate, exfoliated	7.0	LT region	3.8	3.8	0.17	4.2	80	[25]
		HT region			0.17	6.0	110	

fitted parameters of the experimental cases referenced in this paper.

Materials quality is known to influence device mobility. The sulfur vacancy is one of the prevalent defects in monolayer MoS_2. Experimentally repairing sulfur vacancies to improve mobility has been widely studied [23,69]. As stated in Figs. 7(a)–7(c), thiol chemistry was applied to repair sulfur vacancies, and a relationship between material quality and device mobility was built up [23]. The symbols in Fig. 7(a) represent mobility data of an as-exfoliated monolayer MoS_2 transistor. Figures 7(b) and 7(c) represent mobility data of top-side (TS) treated and double-side (DS) treated transistors by self-assembled monolayer (SAM). The mobilities of the three transistors are extracted at $n = 7.1 \times 10^{12}$ cm^{-2}.

For the as-exfoliated transistor, Figs. 7(a) and 7(d) exhibit the fitted curves and the extracted microscopic parameters. The value of N_{tr} (1.05×10^{13} cm^{-2} in the LT region, 1.02×10^{13} cm^{-2} in the HT region) is much higher than n, suggesting that the electron transport of the as-exfoliated transistor is dominantly limited by the LCT effect. In the LT region, the LCT effect plays a dominant role because both μ_{CI} and μ_{ph} are high. Mobility, therefore, increases with T. In the HT region, the mobility shows a decreasing trend due to the increased scattering (μ_{CI}, μ_{ph}, and μ_{SO} decrease with T), while the LCT effect is gradually reducing. It should be noted that $\frac{\partial n_{band}}{\partial n} < 0.5$ over the entire range of temperature, which implies that the electron transport of the as-exfoliated transistor is the LCT-dominated limited mechanism.

The fitted results and extracted parameters of the TS-treated transistor are shown in Figs. 7(b) and 7(e). Compared with the as-exfoliated transistor, the decoupled results of the TS-treated transistor show that the CI scattering limited mobility has a small increment, but the LCT effect is apparently weakened. Specifically, $\frac{\partial n_{band}}{\partial n} > 0.5$ at $T > 80$ K, indicating the CI scattering-dominated limited mechanism. A similar trend can be observed for the extracted parameters. Here, n_{CI} of the TS-treated transistor changes minimally (from 9×10^{11} to 8.8×10^{11} cm^{-2}), but N_{tr} decreased markedly compared with the as-exfoliated transistor (7.4×10^{12} cm^{-2} at the LT region and 6.2×10^{12} cm^{-2} at the HT region). In addition, a discontinuous increase of $\frac{\partial n_{band}}{\partial n}$ occurs at the transition temperature of $T = 100$ K, indicating a reduction in the LCT effect at elevated temperatures. The fitting results indicate that the top surface treatment by SAM effectively reduces N_{tr} but has a smaller effect on n_{CI}.

Figures 7(c) and 7(f) present the fitted results and extracted parameters of the DS-treated transistor. The mobility of the DS-treated transistor was further enhanced compared with the TS-treated transistor, which is mainly due to the overall higher mobility of μ_{CI}. Both the surface and the interface treatment can further reduce n_{CI} compared with the TS-treated transistor (from 8.8×10^{11} to 2.3×10^{11} cm^{-2}). Remarkably, μ_{ph} crosses over μ_{CI} at $T \sim 150$ K, revealing that lattice phonon

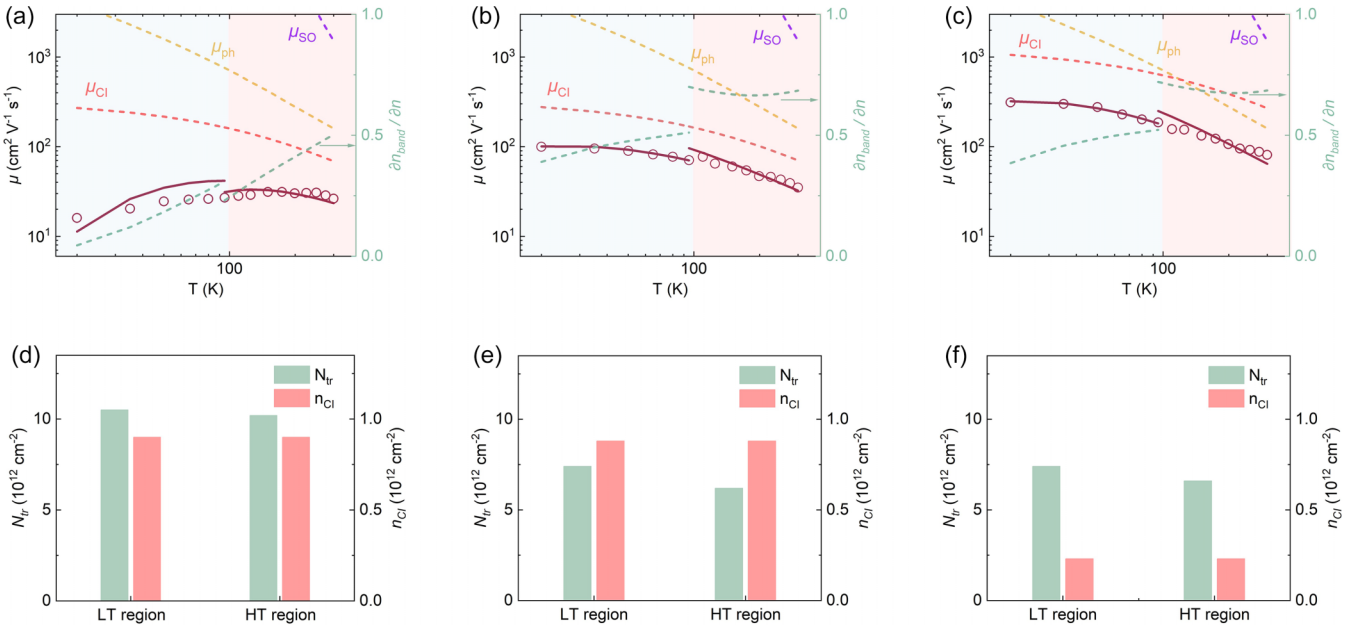

FIG. 7. The μ_{ex}-T relationship (red symbols) [23], the fitted results (red solid lines), and the extracted microscopic parameters (N_{tr} and n_{CI}) of (a) and (d) the as-exfoliated, (b) and (e) the top-side (TS)-exfoliated, and (c) and (f) the double-side (DS)-exfoliated monolayer MoS_2 transistors in the low-temperature (LT) and high-temperature (HT) regions, respectively, at $n = 7.1 \times 10^{12}$ cm^{-2}. The fitted μ_{ph}, μ_{CI}, μ_{SO}, and the localized charge trap (LCT) effect are also shown in (a)–(c) (yellow, pink, violet, and light green dotted lines), respectively.

scattering becomes the dominant limited mechanism after this temperature.

In general, as the thiol repairing strategy progresses, in this paper, we show that thiol chemistry can change the electron transport mechanism. The system gradually transitions from a LCT- to a CI scattering-dominated limited mechanism. Furthermore, the DS-treated transistor exhibits a lattice phonon scattering-dominated limited mechanism at $T > 150$ K.

The case referenced in Figs. 8(a)–8(c) introduces the impact of the interfacial environment on electron transport properties [20,25,34]. Specifically, monolayer MoS_2 was separately encapsulated in Al_2O_3, HfO_2, and hBN. The mobilities are extracted at $n = 1.0 \times 10^{13}$, 7.0×10^{12}, and 7.0×10^{12} cm^{-2}, respectively.

The effects of the interfacial environment on the electron transport of 2D semiconductor materials are complicated. Generally speaking, increasing the dielectric constant of dielectric materials enhances the screening effect of CI centers, which then improves electron transport properties. However, the negative effects of interfaces also possibly arise mainly from CI scattering, SO scattering, and charge trapping attributed to interfacial charge centers, dangling bonds, and adsorbates, respectively. Authors of numerous previous studies have reported the effect of interfaces on electron transport properties from a qualitative perspective [3,25,49,70,71]. For instance, hBN has been a highly promising interface material with the advantages of the well-formed 2D lattice structure, the absence of dangling bonds at the surface, and the negligible surface phonon scattering. In comparison, the common dielectric layers as Al_2O_3 and HfO_2, lattice defects, unsaturated bonds at the interface, and Coulomb impurities or adsorbates, which result in higher n_{CI} and N_{tr} than hBN.

For the Al_2O_3-encapsulated transistor, as shown in Fig. 8(a), the values of $\frac{\partial n_{band}}{\partial n}$ vary between 0.4 and 0.6. At the same time, the value of N_{tr} hangs around n [Fig. 8(d)], suggesting a nonnegligible effect of LCTs. Here, $\frac{\partial n_{band}}{\partial n} > 0.5$ at $T > 40$ K, suggesting CI scattering becomes a dominant limited mechanism among these scattering events. The value of N_{tr} hangs around n [Fig. 8(d)], suggesting a nonnegligible effect of LCT.

For the fitted results of the HfO_2-encapsulated transistor [Figs. 8(b) and 8(e)], the decoupling results show that CI scattering is the noticeable feature in this system. Lattice phonon scattering and SO scattering only act as secondary scattering mechanisms at the HT region and are essentially negligible at the LT region. In addition, the LCT effect is gradually stronger as the temperature increases, which is consistent with the investigated experimental results in the multilayer MoS_2 field-effect transistor [50]. The hypothesized origin is possible since the interface traps were activated as the temperature rose. The extracted parameters show that the values of N_{tr} increase from 5.6×10^{12} to 6.8×10^{12} cm^{-2}.

Figures 8(c) and 8(f) show the fitted curves and the extracted parameters of the hBN-encapsulated transistor. In comparison with the aforementioned two cases, an overall mobility improvement is observed. This is because hBN has a clean interface and absence of dangling bonds for wrapping MoS_2. The low level of n_{CI} (1.7×10^{11} cm^{-2}) in hBN does not cause the reduction of μ_{CI}. It is noteworthy that lattice phonon scattering has replaced CI scattering as the dominant limited mechanism at temperature >50 K. Although we did not consider SO scattering of hBN due to its rigid SO phonons [20], our model fits the experimental results well. In addition, the LCT effect showed a similar decreasing trend to that of the

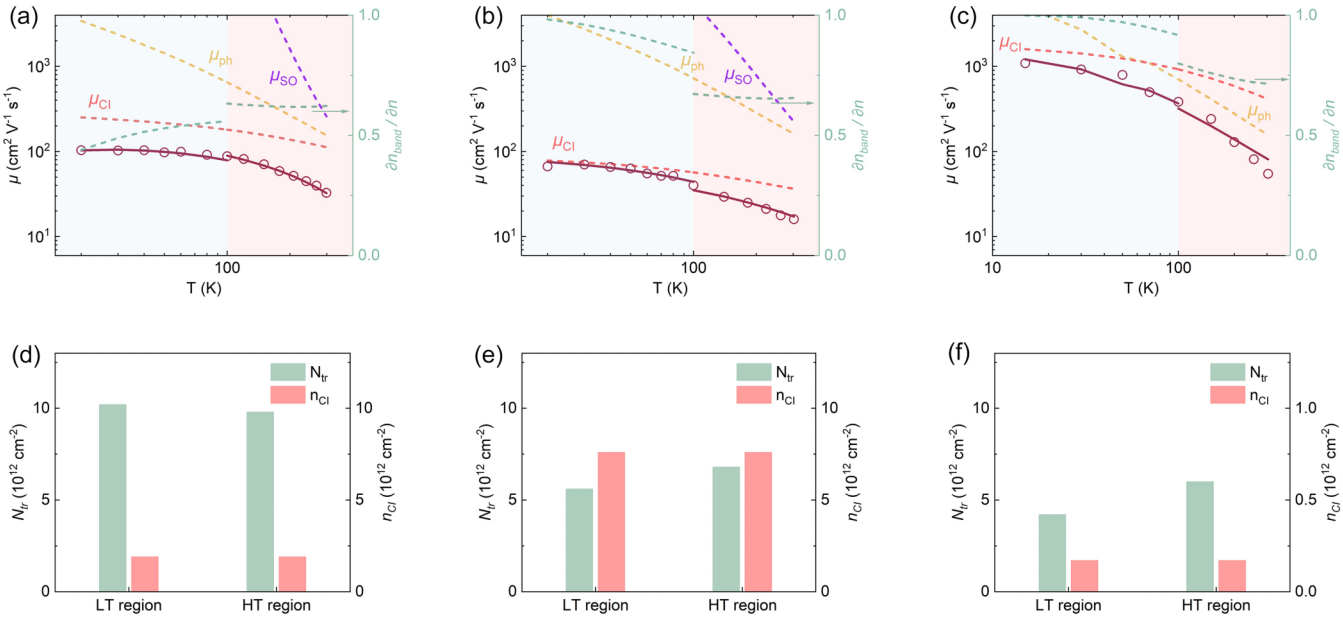

FIG. 8. The μ_{ex}-T relationship (red symbols) [20], the fitted results (red solid lines), and the extracted microscopic parameters (N_{tr} and n_{CI}) for (a) and (d) the Al_2O_3-encapsulated transistor [34] at $n = 1.0 \times 10^{13}\,cm^{-2}$, (b) and (e) the HfO_2-encapsulated transistor [20] at $n = 7.0 \times 10^{12}\,cm^{-2}$, and (c) and (f) the hBN-encapsulated transistor [25] at $n = 7.0 \times 10^{12}\,cm^{-2}$ in the low-temperature (LT) and high-temperature (HT) regions, respectively. The fitted μ_{ph}, μ_{CI}, μ_{SO}, and the localized charge trap (LCT) effect are also shown in (a)–(c) (yellow, pink, violet, and light green dotted lines), respectively.

HfO_2-encapsulated transistor, which may also be related to the thermal activation of interfacial traps.

Theoretically, higher dielectric constants are better for device mobility (μ_{ex}), but a variety of aspects affect μ_{ex}. If one wants to study the dielectric constant effect alone, an ideal device system with better device parameters control needs to be established.

IV. CONCLUSIONS

In summary, we have developed a theoretical model by reevaluating μ_{ph} and the LCT effect. The model can theoretically decouple the mobility-temperature relationships and study the electron transport mechanisms of monolayer MoS_2 transistors. The theoretical model exhibits two noteworthy features: (1) The improved calculation method for μ_{ph} was integrated, thereby avoiding the overestimation of other scattering and the LCT effect. (2) Temperature-dependent parameters of the LCT effect were proposed. In the analyzed cases for the improvement of material quality and modulation of interfacial environment, the developed model achieved well-fitted results for both the LCT- and the different scattering-dominated limited mechanisms. The systematic theoretical analysis contributes deep insights for comprehending electron transport mechanisms and guiding device performance improvement in monolayer MoS_2 transistors.

ACKNOWLEDGMENTS

This paper is supported by the National Natural Science Foundation of China (Grant No. 52102183). The computations of μ_{ph} in this paper were run on the Magic Cube-III cluster supported by Shanghai Supercomputer Center. The authors thank Dr. Tiesheng Wang, Dr. Saiyu Bu, Dr. Gang Zhang, and Dr. Zhunyong Ong for their support and professional guidance in the initial studies.

[1] S. Wang, X. Liu, M. Xu, L. Liu, D. Yang, and P. Zhou, Two-dimensional devices and integration towards the silicon lines, Nat. Mater. **21**, 1225 (2022).

[2] B. Radisavljevic, A. Radenovic, J. Brivio, V. Giacometti, and A. Kis, Single-layer MoS_2 transistors, Nat. Nanotechnol. **6**, 147 (2011).

[3] B. Radisavljevic and A. Kis, Mobility engineering and a metal-insulator transition in monolayer MoS_2, Nat. Mater. **12**, 815 (2013).

[4] K. Kang, S. Xie, L. Huang, Y. Han, P. Y. Huang, K. F. Mak, C.-J. Kim, D. Muller, and J. Park, High-mobility three-atom-thick semiconducting films with wafer-scale homogeneity, Nature (London) **520**, 656 (2015).

[5] A. Sebastian, R. Pendurthi, T. H. Choudhury, J. M. Redwing, and S. Das, Benchmarking monolayer MoS_2 and WS_2 field-effect transistors, Nat. Commun. **12**, 693 (2021).

[6] Y. Liu, X. Duan, H.-J. Shin, S. Park, Y. Huang, and X. Duan, Promises and prospects of two-dimensional transistors, Nature (London) **591**, 43 (2021).

[7] K. S. Novoselov, A. Mishchenko, A. Carvalho, and A. H. Castro Neto, 2D materials and van der Waals heterostructures, Science **353**, aac9439 (2016).

[8] S. Manzeli, D. Ovchinnikov, D. Pasquier, O. V. Yazyev, and A. Kis, 2D transition metal dichalcogenides, Nat. Rev. Mater. **2**, 17033 (2017).

[9] M. Chhowalla, D. Jena, and H. Zhang, Two-dimensional semiconductors for transistors, Nat. Rev. Mater. **1**, 16052 (2016).

[10] S. Das, A. Sebastian, E. Pop, C. J. McClellan, A. D. Franklin, T. Grasser, T. Knobloch, Y. Illarionov, A. V. Penumatcha, J. Appenzeller *et al.*, Transistors based on two-dimensional materials for future integrated circuits, Nat. Electron. **4**, 786 (2021).

[11] J. Qiao, S. Wang, Z. Wang, C. He, S. Zhao, X. Xiong, S. Wang, X. Zhang, and X. Tao, Ultrasensitive and broadband all-optically controlled THz modulator based on $MoTe_2$/Si van der Waals heterostructure, Adv. Opt. Mater. **8**, 2000160 (2020).

[12] H. Hinton, H. Jang, W. Wu, M. H. Lee, M. Seol, H. J. Shin, S. Park, and D. Ham, A 200×256 image sensor heterogeneously integrating a 2D nanomaterial-based photo-FET array and CMOS time-to-digital converters, in *2022 IEEE International Solid-State Circuits Conference* (IEEE, 2022), p. 1.

[13] V. K. Sangwan, H.-S. Lee, H. Bergeron, I. Balla, M. E. Beck, K.-S. Chen, and M. C. Hersam, Multi-terminal memtransistors from polycrystalline monolayer molybdenum disulfide, Nature (London) **554**, 500 (2018).

[14] F. Zhang, H. Zhang, S. Krylyuk, C. A. Milligan, Y. Zhu, D. Y. Zemlyanov, L. A. Bendersky, B. P. Burton, A. V. Davydov, and J. Appenzeller, Electric-field induced structural transition in vertical $MoTe_2$- and $Mo_{1-x}W_xTe_2$-based resistive memories, Nat. Mater. **18**, 55 (2019).

[15] K. Zhu, S. Pazos, F. Aguirre, Y. Shen, Y. Yuan, W. Zheng, O. Alharbi, M. A. Villena, B. Fang, X. Li *et al.*, Hybrid 2D-CMOS microchips for memristive applications, Nature (London) **618**, 57 (2023).

[16] C. Dai, Y. Liu, and D. Wei, Two-dimensional field-effect transistor sensors: The road toward commercialization, Chem. Rev. **122**, 10319 (2022).

[17] D. Sarkar, W. Liu, X. Xie, A. C. Anselmo, S. Mitragotri, and K. Banerjee, MoS_2 field-effect transistor for next-generation label-free biosensors, ACS Nano **8**, 3992 (2014).

[18] K. Kaasbjerg, K. S. Thygesen, and A.-P. Jauho, Acoustic phonon limited mobility in two-dimensional semiconductors: Deformation potential and piezoelectric scattering in monolayer MoS_2 from first principles, Phys. Rev. B **87**, 235312 (2013).

[19] H. Liu, M. Si, S. Najmaei, A. T. Neal, Y. Du, P. M. Ajayan, J. Lou, and P. D. Ye, Statistical study of deep submicron dual-gated field-effect transistors on monolayer chemical vapor deposition molybdenum disulfide films, Nano Lett. **13**, 2640 (2013).

[20] W. Zhang, B. Liang, J. Tang, J. Chen, Q. Wan, Y. Shi, and S. Li, Performance limits of all-wrapped monolayer MoS_2 transistors, Sci. Bull. **68**, 2025 (2023).

[21] H. Xu, H. Zhang, Z. Guo, Y. Shan, S. Wu, J. Wang, W. Hu, H. Liu, Z. Sun, C. Luo *et al.*, High-performance wafer-scale MoS_2 transistors toward practical application, Small **14**, 1803465 (2018).

[22] S.-L. Li, K. Tsukagoshi, E. Orgiu, and P. Samorì, Charge transport and mobility engineering in two-dimensional transition metal chalcogenide semiconductors, Chem. Soc. Rev. **45**, 118 (2016).

[23] Z. Yu, Y. Pan, Y. Shen, Z. Wang, Z.-Y. Ong, T. Xu, R. Xin, L. Pan, B. Wang, L. Sun *et al.*, Towards intrinsic charge transport in monolayer molybdenum disulfide by defect and interface engineering, Nat. Commun. **5**, 5290 (2014).

[24] Z. Yu, Z. Y. Ong, Y. Pan, Y. Cui, R. Xin, Y. Shi, B. Wang, Y. Wu, T. Chen, Y. W. Zhang *et al.*, Realization of room-temperature phonon-limited carrier transport in monolayer MoS_2 by dielectric and carrier screening, Adv. Mater. **28**, 547 (2016).

[25] X. Cui, G.-H. Lee, Y. D. Kim, G. Arefe, P. Y. Huang, C.-H. Lee, D. A. Chenet, X. Zhang, L. Wang, F. Ye *et al.*, Multi-terminal transport measurements of MoS_2 using a van der Waals heterostructure device platform, Nat. Nanotechnol. **10**, 534 (2015).

[26] N. Huo, Y. Yang, Y.-N. Wu, X.-G. Zhang, S. T. Pantelides, and G. Konstantatos, High carrier mobility in monolayer CVD-grown MoS_2 through phonon suppression, Nanoscale **10**, 15071 (2018).

[27] Z. Yu, Z.-Y. Ong, S. Li, J.-B. Xu, G. Zhang, Y.-W. Zhang, Y. Shi, and X. Wang, Analyzing the carrier mobility in transition-metal dichalcogenide MoS_2 field-effect transistors, Adv. Funct. Mater. **27**, 1604093 (2017).

[28] V. K. Sangwan and M. C. Hersam, Electronic transport in two-dimensional materials, Annu. Rev. Phys. Chem. **69**, 299 (2018).

[29] S. L. Li, K. Wakabayashi, Y. Xu, S. Nakaharai, K. Komatsu, W. W. Li, Y. F. Lin, A. Aparecido-Ferreira, and K. Tsukagoshi, Thickness-dependent interfacial coulomb scattering in atomically thin field-effect transistors, Nano Lett. **13**, 3546 (2013).

[30] N. Ma and D. Jena, Charge scattering and mobility in atomically thin semiconductors, Phys. Rev. X **4**, 011043 (2014).

[31] W. Zhu, T. Low, Y.-H. Lee, H. Wang, D. B. Farmer, J. Kong, F. Xia, and P. Avouris, Electronic transport and device prospects of monolayer molybdenum disulphide grown by chemical vapour deposition, Nat. Commun. **5**, 3087 (2014).

[32] M.-K. Joo, B. H. Moon, H. Ji, G. H. Han, H. Kim, G. Lee, S. C. Lim, D. Suh, and Y. H. Lee, Electron excess doping and effective Schottky barrier reduction on the MoS_2/h-BN heterostructure, Nano Lett. **16**, 6383 (2016).

[33] L. Cheng and Y. Liu, What limits the intrinsic mobility of electrons and holes in two dimensional metal dichalcogenides? J. Am. Chem. Soc. **140**, 17895 (2018).

[34] S. Ju, B. Liang, J. Zhou, D. Pan, Y. Shi, and S. Li, Coulomb screening and scattering in atomically thin transistors across dimensional crossover, Nano Lett. **22**, 6671 (2022).

[35] K. Kaasbjerg, K. S. Thygesen, and K. W. Jacobsen, Phonon-limited mobility in n-type single-layer MoS_2 from first principles, Phys. Rev. B **85**, 115317 (2012).

[36] T. Gunst, T. Markussen, K. Stokbro, and M. Brandbyge, First-principles method for electron-phonon coupling and electron mobility: Applications to two-dimensional materials, Phys. Rev. B **93**, 035414 (2016).

[37] J. Backman, Y. Lee, and M. Luisier, Electron-phonon calculations using a Wannier-based supercell approach: Applications to the monolayer MoS_2 mobility, Solid-State Electron. **198**, 108461 (2022).

[38] X. Li, J. T. Mullen, Z. Jin, K. M. Borysenko, M. Buongiorno Nardelli, and K. W. Kim, Intrinsic electrical transport properties of monolayer silicene and MoS_2 from first principles, Phys. Rev. B **87**, 115418 (2013).

[39] O. D. Restrepo, K. E. Krymowski, J. Goldberger, and W. Windl, A first principles method to simulate electron mobilities in 2D materials, New J. Phys. **16**, 105009 (2014).

[40] W. Li, Electrical transport limited by electron-phonon coupling from Boltzmann transport equation: An *ab initio* study of Si, Al, and MoS_2, Phys. Rev. B **92**, 075405 (2015).

[41] Y. Zhao, Z. Dai, C. Zhang, C. Lian, S. Zeng, G. Li, S. Meng, and J. Ni, Intrinsic electronic transport and thermoelectric power factor in *n*-type doped monolayer MoS_2, New J. Phys. **20**, 043009 (2018).

[42] F. Guo, Z. Liu, M. Zhu, and Y. Zheng, Effects of uniaxial tensile strain on the electron-phonon scattering limited carrier mobility in an *n*-type monolayer MoS_2 at room temperature: First-principles calculations, J. Phys.: Condens. Matter **31**, 295502 (2019).

[43] F. Guo, Z. Liu, M. Zhu, and Y. Zheng, Electron-phonon scattering limited hole mobility at room temperature in a MoS_2 monolayer: First-principles calculations, Phys. Chem. Chem. Phys. **21**, 22879 (2019).

[44] G. Gaddemane, S. Gopalan, M. L. Van de Put, and M. V. Fischetti, Limitations of *ab initio* methods to predict the electronic-transport properties of two-dimensional semiconductors: The computational example of 2*H*-phase transition metal dichalcogenides, J. Comput. Electron. **20**, 49 (2021).

[45] J. J. Zhou, J. Park, I. T. Lu, I. Maliyov, X. Tong, and M. Bernardi, PERTURBO: A software package for *ab initio* electron-phonon interactions, charge transport and ultrafast dynamics, Comput. Phys. Commun. **264**, 107970 (2021).

[46] S. Song, J.-H. Yang, and X.-G. Gong, Abnormally weak intervalley electron scattering in MoS_2 monolayer: Insights from the matching between electron and phonon bands, Nanoscale **14**, 12007 (2022).

[47] H. Qiu, T. Xu, Z. Wang, W. Ren, H. Nan, Z. Ni, Q. Chen, S. Yuan, F. Miao, F. Song *et al.*, Hopping transport through defect-induced localized states in molybdenum disulphide, Nat. Commun. **4**, 2642 (2013).

[48] Y. Y. Illarionov, G. Rzepa, M. Waltl, T. Knobloch, A. Grill, M. M. Furchi, T. Mueller, and T. Grasser, The role of charge trapping in MoS_2/SiO_2 and MoS_2/hBN field-effect transistors, 2D Mater. **3**, 035004 (2016).

[49] M.-K. Joo, B. H. Moon, H. Ji, G. H. Han, H. Kim, G. Lee, S. C. Lim, D. Suh, and Y. H. Lee, Understanding Coulomb scattering mechanism in monolayer MoS_2 channel in the presence of h-BN buffer layer, ACS Appl. Mater. Interfaces **9**, 5006 (2017).

[50] Y. Park, H. W. Baac, J. Heo, and G. Yoo, Thermally activated trap charges responsible for hysteresis in multilayer MoS_2 field-effect transistors, Appl. Phys. Lett. **108**, 083102 (2016).

[51] See Supplemental Material at http://link.aps.org/supplemental/10.1103/PhysRevB.110.115414 for the calculation details of the lattice phonon scattering limited mobility ($\mu_{\rm ph}$), the Coulomb-impurity scattering limited mobility ($\mu_{\rm CI}$), the surface optical phonon scattering limited mobility ($\mu_{\rm SO}$), and the LCT effect; interpolated electronic and phononic structures of monolayer MoS_2 by the PERTURBO code; the fitted $\mu_{\rm SO}$ with T varying from 20 to 143 K at $n = 7.6 \times 10^{12}$ cm^{-2} [26]; a description of the device parameter selection; and a statement of integral grid sufficiency in the calculation process of $\mu_{\rm ph}$ by the PERTURBO code.

[52] S. Baroni, S. de Gironcoli, A. Dal Corso, and P. Giannozzi, Phonons and related crystal properties from density-functional perturbation theory, Rev. Mod. Phys. **73**, 515 (2001).

[53] J. H. Davies, *The Physics of Low-Dimensional Semiconductors: An Introduction* (Cambridge University Press, Cambridge, 1997).

[54] P. Giannozzi, O. Andreussi, T. Brumme, O. Bunau, M. Buongiorno Nardelli, M. Calandra, R. Car, C. Cavazzoni, D. Ceresoli, M. Cococcioni *et al.*, Advanced capabilities for materials modelling with QUANTUM ESPRESSO, J. Phys. Condens. Matter **29**, 465901 (2017).

[55] P. Giannozzi, S. Baroni, N. Bonini, M. Calandra, R. Car, C. Cavazzoni, D. Ceresoli, G. L. Chiarotti, M. Cococcioni, I. Dabo *et al.*, QUANTUM ESPRESSO: A modular and open-source software project for quantum simulations of materials, J. Phys. Condens. Matter **21**, 395502 (2009).

[56] P. Giannozzi, O. Baseggio, P. Bonfà, D. Brunato, R. Car, I. Carnimeo, C. Cavazzoni, S. de Gironcoli, P. Delugas, F. Ferrari Ruffino *et al.*, QUANTUM ESPRESSO toward the exascale, J. Chem. Phys. **152**, 154105 (2020).

[57] N. Marzari and D. Vanderbilt, Maximally localized generalized Wannier functions for composite energy bands, Phys. Rev. B **56**, 12847 (1997).

[58] A. A. Mostofi, J. R. Yates, G. Pizzi, Y.-S. Lee, I. Souza, D. Vanderbilt, and N. Marzari, An updated version of WANNIER90: A tool for obtaining maximally-localised Wannier functions, Comput. Phys. Commun. **185**, 2309 (2014).

[59] Z. Y. Ong and M. V. Fischetti, Charged impurity scattering in top-gated graphene nanostructures, Phys. Rev. B **86**, 121409(R) (2012).

[60] Z. Y. Ong and M. V. Fischetti, Mobility enhancement and temperature dependence in top-gated single-layer MoS_2, Phys. Rev. B **88**, 165316 (2013).

[61] J. P. Perdew, K. Burke, and M. Ernzerhof, Generalized gradient approximation made simple, Phys. Rev. Lett. **77**, 3865 (1996).

[62] G. Pizzi, V. Vitale, R. Arita, S. Blügel, F. Freimuth, G. Géranton, M. Gibertini, D. Gresch, C. Johnson, T. Koretsune *et al.*, WANNIER90 as a community code: New features and applications, J. Condens. Matter Phys. **32**, 165902 (2020).

[63] T. Sohier, M. Calandra, and F. Mauri, Two-dimensional Fröhlich interaction in transition-metal dichalcogenide monolayers: Theoretical modeling and first-principles calculations, Phys. Rev. B **94**, 085415 (2016).

[64] T. Sohier, M. Calandra, and F. Mauri, Density functional perturbation theory for gated two-dimensional heterostructures: Theoretical developments and application to flexural phonons in graphene, Phys. Rev. B **96**, 075448 (2017).

[65] I. Souza, N. Marzari, and D. Vanderbilt, Maximally localized Wannier functions for entangled energy bands, Phys. Rev. B **65**, 035109 (2001).

[66] M. J. van Setten, M. Giantomassi, E. Bousquet, M. J. Verstraete, D. R. Hamann, X. Gonze, and G. M. Rignanese, The PSEUDODOJO: Training and grading a 85 element optimized norm-conserving pseudopotential table, Comput. Phys. Commun. **226**, 39 (2018).

[67] H. Xie, H. Alves, and A. F. Morpurgo, Quantitative analysis of density-dependent transport in tetramethyltetraselenafulvalene single-crystal transistors: Intrinsic properties and trapping, Phys. Rev. B **80**, 245305 (2009).

[68] M. Y. Chan, K. Komatsu, S.-L. Li, Y. Xu, P. Darmawan, H. Kuramochi, S. Nakaharai, A. Aparecido-Ferreira, K.

Watanabe, T. Taniguchi *et al.*, Suppression of thermally activated carrier transport in atomically thin MoS_2 on crystalline hexagonal boron nitride substrates, Nanoscale **5**, 9572 (2013).

[69] S. Najmaei, X. Zou, D. Er, J. Li, Z. Jin, W. Gao, Q. Zhang, S. Park, L. Ge, S. Lei *et al.*, Tailoring the physical properties of molybdenum disulfide monolayers by control of interfacial chemistry, Nano Lett. **14**, 1354 (2014).

[70] H. Schmidt, S. Wang, L. Chu, M. Toh, R. Kumar, W. Zhao, A. H. Castro Neto, J. Martin, S. Adam, B. Özyilmaz *et al.*, Transport properties of monolayer MoS_2 grown by chemical vapor deposition, Nano Lett. **14**, 1909 (2014).

[71] S. M. Shinde, T. Das, A. T. Hoang, B. K. Sharma, X. Chen, and J.-H. Ahn, Surface-functionalization-mediated direct transfer of molybdenum disulfide for large-area flexible devices, Adv. Funct. Mater. **28**, 1706231 (2018).